

Modeling the Saddle-like GeV–TeV Spectrum of HESS J1809–193: γ -Rays Arising from Reverse-Shocked Pulsar Wind Nebula?

JIAXU SUN ¹, YANG CHEN ^{1,2}, YIWEI BAO ^{3,4}, XIAO ZHANG ⁵, AND XIN ZHOU ⁶

¹*School of Astronomy & Space Science, Nanjing University, 163 Xianlin Avenue, Nanjing 210023, China*

²*Key Laboratory of Modern Astronomy and Astrophysics, Nanjing University, Ministry of Education, Nanjing 210023, China*

³*Tsung-Dao Lee Institute, Shanghai Jiao Tong University, Shanghai 201210, China*

⁴*School of Physics and Astronomy, Shanghai Jiao Tong University, Shanghai 200240, China*

⁵*School of Physics and Technology, Nanjing Normal University, Nanjing, 210023, Jiangsu, People's Republic of China*

⁶*Purple Mountain Observatory and Key Laboratory of Radio Astronomy, Chinese Academy of Sciences, 10 Yuanhua Road, Nanjing 210023, China*

ABSTRACT

Evolution of pulsar wind nebulae (PWNe) could be expected to leave imprints in γ -rays. We suggest that intriguing GeV–TeV spectral energy distribution (SED) of HESS J1809–193 and Fermi-LAT source J1810.3–1925e is very likely to be the γ -ray signature of PWN J1809–193 in light of the scenario that the PWN was struck by the reverse shock of the parent supernova remnant. Based on evolutionary theory of PWNe, we consider that, when the PWN was disrupted during collision by the reverse shock, some very high-energy electrons escaped impulsively. The remaining electrons stayed in the relic PWN, which was displaced from the pulsar. The very high-energy part of the remaining electrons were depleted by the strong magnetic field that was enhanced by the reverse shock compression in the reverberation stage, leaving the other part of them generating GeV emission. The particles injected from the pulsar after the disruption enter the relic PWN through the newly formed tunnel called the cocoon. The γ -ray emission from the escaped electrons can account for the TeV spectrum of component A of HESS J1809–193 or the TeV halo, while the electrons remaining after disruption can account for the GeV spectrum of J1810.3–1925e. Thus, combination of contributions from these two populations of electrons naturally reproduces the saddle-like SED of HESS J1809–193 and J1810.3–1925e from 5 GeV to 30 TeV, together with the spectral hardening around 100 GeV. We also show that the post-disruption injection of electrons can explain the spectrum of the relatively faint γ -ray emission of component B of HESS J1809–193.

Keywords: Supernova remnants, Pulsar wind nebulae, Gamma-ray sources, Cosmic rays

1. INTRODUCTION

Recent years have witnessed the significant advance in the studies of pulsar wind nebulae (PWNe) and supernova remnants (SNRs) by mutliwavelength (up to ultrahigh energy) observations, which contributes to our understanding of the origin of high energy cosmic rays and γ -ray emissions in the Galaxy. However, due to irregular spectral characteristics and complicated distribution of objects in the field of view, the nature of many very high energy (VHE) γ -ray sources remains uncertain.

In this paper, we discuss the intriguing extended VHE source HESS J1809–193 with $\sim 0^\circ.62$ in semi-major axis and $e = 0.824$ (H. E. S. S. Collaboration et al. 2023). which is situated in a region rich with potential astrophysical counterparts and exhibits distinct spectral properties. The source was first identified by H.E.S.S. during a Galactic Plane Survey (Aharonian et al. 2007) and later resolved into two components (A and B) by H. E. S. S. Collaboration et al. (2023). Component A is extended, exhibiting a spectral cut-off at ~ 13 TeV, and component B is compact, showing

no clear spectral cut-off. Analysis of Fermi-LAT data confirmed the presence of an extended source, J1810.3–1925e, which appears to be related to component A of HESS J1809–193 in view of its location and morphology (H. E. S. S. Collaboration et al. 2023). The region contains several pulsars, SNRs, and molecular clouds, which makes it difficult to identify the exact origin of the γ -rays. Three noticeable pulsars, the transient X-ray magnetar XTE J1810–197 (Alford & Halpern 2016), PSR J1811–1925 (with energy loss rate 6.4×10^{36} erg s⁻¹, at distance $d \sim 5$ kpc (Aharonian et al. 2007)), and PSR J1809–1917 (with 1.8×10^{36} erg s⁻¹ and characteristic age $\tau_c = 51.4$ kyr, at $d \sim 3.3$ kpc (Aharonian et al. 2007)), are located in this region. Based on the existing observational results, the γ -ray source HESS J1809–193 is suggested to be unrelated to magnetar J1810–197 (Maan et al. 2022) and PSR J1811–1925 along with its wind nebula (H. E. S. S. Collaboration et al. 2023). Thus PSR J1809–1917 stands out to be the most plausible candidate for the origin of the γ -rays. PSR J1809–1917 powers an X-ray PWN (hereafter PWN J1809–193) that spans an angular size around $\sim 0^\circ.3$ (Kargaltsev & Pavlov 2007; Anada et al. 2010; Klingler et al. 2018, 2020; Abeysekara et al. 2020a). The extended emission of HESS J1809–193 also overlaps with two known SNRs, G011.1+00.1 and G011.0–00.0, but there is no clear evidence of association with either G011.0–00.0 or G011.0+00.1 (Klingler et al. 2018, 2020; H. E. S. S. Collaboration et al. 2023). HAWC has detected VHE γ -ray emission from HESS J1809–193, with energies exceeding 56 TeV and potentially extending beyond 100 TeV (Abeysekara et al. 2020b; Goodman 2022; Albert et al. 2024), establishing this source as one of the most energetic objects in the TeV range. Chandra observations revealed a faint diffuse X-ray emission that stretches to the south of compact part of PWN harboring PSR J1809–1917 and a bright cocoon-like structure along the central axis of the extended part of PWN (Klingler et al. 2020). Fermi-LAT Fermi-LAT shows an extended GeV emission overlapping the TeV γ -ray emission. However, the GeV emission spectrum of the associated source J1810.3–1925e cannot connect smoothly to the TeV spectrum of component A of HESS J1809–193, implying the need for a spectral hardening around 100 GeV (Araya 2018; Albert et al. 2024). The TeV emission of HESS J1809–193 covers a broader area than the GeV emission (H. E. S. S. Collaboration et al. 2023).

Many studies have explored both leptonic and hadronic scenarios for HESS J1809–193. The discovery paper (Aharonian et al. 2007) and follow-up works (Komin et al. 2008; Renaud et al. 2008) suggested that the PWN around PSR J1809–1917 could explain the TeV emission through a leptonic scenario. In H. E. S. S. Collaboration et al. (2023), component A is considered to be likely caused by inverse Compton (IC) emission from old electrons that form a halo around the PWN; and component B could be connected to either the PWN or the SNR and molecular clouds. However, it later confronts the aforementioned non-smoothed connection of GeV-TeV spectra. Current leptonic models, including that utilizing HAWC data, could not accommodate the spectrum of Fermi-LAT source J1810.3–1925e below ~ 10 GeV (H. E. S. S. Collaboration et al. 2023; Albert et al. 2024).

On the other hand, some studies proposed hadronic interpretations for the emission from the HESS J1809–193 region. Radio observations at 330 MHz and 1456 MHz revealed two SNRs, G011.1+00.1 (10' in angular diameter) and G011.0–00.0 (11' in angular diameter), in the region (Green 2004; Brogan et al. 2006; Castelletti et al. 2016). Castelletti et al. (2016), Araya (2018), Voisin et al. (2019), and Boxi & Gupta (2024) proposed that cosmic rays accelerated by SNR G011.0–00.0 interacting with molecular clouds could be responsible for the emission. However, a lack of correlation between component A and the gas present in the region disfavors a hadronic interpretation for this component, and attributing component B to hadronic explanation would leave the X-ray PWN without a counterpart at TeV energies (component A being attributed to electrons injected long ago only) (H. E. S. S. Collaboration et al. 2023).

γ -ray emission from the HESS J1809–193 region exhibits spectral hardening in the GeV band and a saddle-like feature in the GeV–TeV range, which is reminiscent of another well-known PWN system, Vela X, which also exhibits a depression around 100 GeV in the GeV–TeV spectral energy distribution (SED) (Tibaldo et al. 2018). The SED of the Vela X PWN can be interpreted (Bao et al. 2019; Bao & Chen 2019) according to current evolutionary theory of PWNe (Gaensler & Slane 2006) and hydrodynamic simulation of the Vela X PWN (Slane et al. 2018). When the reverse shock from the SNR travels backwards, it encounters the expanding PWN, compressing it. The PWN then experiences reverberation, disrupted or even crushed, and very high-energy electrons escape. Simultaneously, the compression of the PWN enhances the internal magnetic field, depleting very high-energy electrons in the relic PWN through radiation losses. This process can naturally produce a saddle-featured spectrum with two populations of electrons: the electrons left in the compressed relic PWN generate GeV emission, while very high-energy electrons escaped from the original PWN at disruption generate diffusive TeV emission.

In this paper, we suggest that the J1809–193 PWN may be another example, next to the Vela X PWN, producing saddle-like GeV-TeV SED as a result of PWN evolution.

2. MODELLING THE SED OF HESS J1809–193

2.1. About structure and evolution of PWN J1809–193

In X-rays (0.5–8 keV), PWN J1809–193 is mainly comprised of a compact nebula immediately surrounding the pulsar and an extended nebula in the southwest (Klingler et al. 2020). The PWN, $\gtrsim 10'$ in size (Li et al. 2023), is approximately symmetric about the northeast-southwest oriented central axis, and there is a short (probably by projection) bright bar-like structure, connecting with the compact nebula, largely oriented along the axis (see Figure 6 in Klingler et al. 2020). Such a morphology is consistent with a PWN that SNR reverse shock has swept over and compressed (Gaensler & Slane 2006; Slane et al. 2018). The bar-like structure is very similar to the “cocoon” in the Vela X PWN (Slane et al. 2018). The extended GeV emission region, which was revealed from the Fermi-LAT observation and is represented by a disk model with a radius of about $\sim 0^\circ.3$ (Araya 2018) or 8 pc at $d \sim 3.3$ kpc, may correspond to the relic PWN after the passage of reverse shock. The X-ray emitting part of the PWN is now projected inside this region, but the tunnel between the pulsar and the relic PWN, represented by the bar-like structure or “cocoon”, needs not perfectly align with the line between the pulsar and the center of the relic PWN, like the case of the PWN in SNR G327.1–1.1 due to addition of the transverse component of the pulsar’s proper motion (see Figure 3 in Gaensler & Slane 2006; Temim et al. 2015).

According to the hydrodynamic simulation of PWN evolution (Gaensler & Slane 2006; Temim et al. 2015; Slane et al. 2018), it can be envisaged that the parent SNR of PWN J1809–193 was born in an interstellar environment with a density gradient. The reverse shock moved inwards from the side with relatively dense ambient medium first collided the PWN, one-sidedly compressing it, and created a trail behind the pulsar. In the reverberation stage of interaction with reverse shock, the PWN was disrupted, and a small portion of the high-energy particles, which was uncompressed in the trail, impulsively escaped from the PWN into the surrounding region, forming the observed extended TeV halo. Meanwhile, most part of high energy particles remained in the relic PWN that was driven to the other side. The very high-energy part of the remaining electrons were burnt off by the strong magnetic field that was enhanced by the compression in a short timescale $\sim 10(B/10^2 \mu\text{G})^{-2} (E/10^2 \text{ TeV})^{-1} \text{ yr}$ (where E denotes the energy of electron) (Hinton et al. 2011). The other remaining electrons generate the GeV emission. With the passage of the reverse shock, a compact nebula enveloping the pulsar and a trailing part appeared, while a cocoon was formed as a tunnel for subsequent particle injection from the pulsar to the relic PWN.

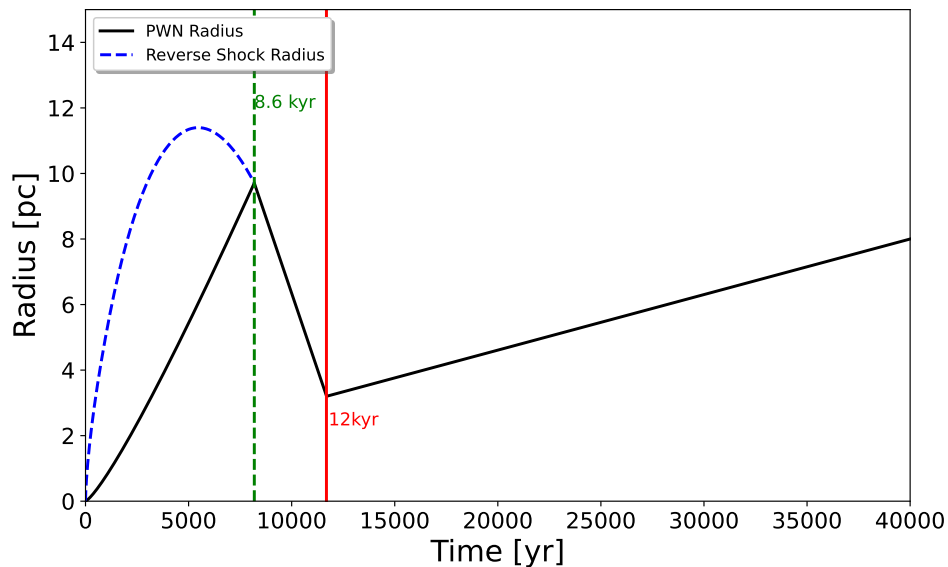


Figure 1. The evolution of the reverse shock radius and the pulsar wind nebula (PWN) radius over time. The green line indicates $t = 8.6$ kyr, where the interaction begins leading to the compression of the PWN. The red line indicates the characteristic time of disruption $t_{\text{disr}} = 12$ kyr.

Figure 1 shows that PWN J1809–193 was hit by the reverse shock at ~ 8.6 kyr and was compressed to a minimum size at ~ 12 kyr, as calculated according to Truelove & McKee (1999) (also see relevant algorithm described in Bao

& Chen (2019)), with the supernova explosion energy $E_{\text{SN}} \sim 10^{51}$ erg and ejecta mass $M_{\text{ej}} \sim 5M_{\odot}$ assumed and the ambient gas density $n_{\text{ISM}} \sim 0.04 \text{ cm}^{-3}$ fitted from the evolution of the relic PWN. After the hitting, the first compression is believed to be the most significant (Bandiera et al. 2023), particles' escape is assumed to happen around the moment the PWN was compressed to the maximum extent (namely $t_{\text{disr}} \sim 12$ kyr), and the subsequent reverberations may not occur because the PWN lacks the power to re-expand the interface (Bandiera et al. 2020). Therefore, this work considers only one complete reverberation cycle. For the expansion after the compression, we assume that the relic PWN adiabatically expanded at a constant velocity calculated from the balance between PWN and outer pressure following the treatment in Bao & Chen (2019). The age of the remnant $T_{\text{age}} \sim 40$ kyr is obtained from the dynamic calculation so as for the relic PWN to reach a radial extent of 8 pc presently.

2.2. Escaped particles and the TeV halo

Following H. E. S. S. Collaboration et al. (2023), we adopt the single power law distribution, as written below, for the escaped very high energy particles to explain the spectrum of the TeV halo:

$$q_{\text{inj}}(\gamma) = q_{\text{A}} \delta(t_{\text{dif}}) \left(\frac{\gamma}{10^7} \right)^{-\alpha_{\text{A}}}, \quad (1)$$

where q_{A} is the injection constant for the electrons with $\gamma = 10^7$, and $\delta(t_{\text{dif}})$ is delta function. The transport of TeV γ -ray emitting electrons that are injected at disruption can be described by the following equation:

$$\frac{\partial}{\partial t_{\text{dif}}} f(\gamma, r, t_{\text{dif}}) = \frac{D(\gamma)}{r^2} \frac{\partial}{\partial r} r^2 \frac{\partial}{\partial r} f(\gamma, r, t_{\text{dif}}) + \frac{\partial}{\partial \gamma} (Pf) + q_{\text{inj}}(\gamma, t_{\text{dif}}), \quad (2)$$

where $f(\gamma, r, t_{\text{dif}})$ denotes the electron distribution function, r the radial distance from the center of the TeV halo, $t_{\text{dif}} = t - t_{\text{disr}}$ the time after the injection, P the radiation energy loss rate, $q_{\text{inj}}(\gamma, t)$ the electron injection rate (differential number per unit volume per unit time), and $D(\gamma) = D_0 (\gamma/\gamma_{40\text{TeV}})^{\delta}$ the energy-dependent diffusion coefficient (with D_0 the diffusion coefficient normalized at Lorentz factor $\gamma_{40\text{TeV}}$ with 40 TeV and δ the energy dependence index of diffusion). The analytical solution to Equation 2 is given by

$$f(\gamma, r, t_{\text{dif}}) = \begin{cases} \frac{\gamma_t^2 q_{\text{inj}}(\gamma_t, t_{\text{dif}})}{\gamma^2 \pi^{3/2} r_{\text{dif}}^3} \exp\left(-\frac{r^2}{r_{\text{dif}}^2}\right) & \gamma \leq \gamma_{\text{max}}, \\ 0 & \gamma > \gamma_{\text{max}}, \end{cases} \quad (3)$$

where $r_{\text{dif}}(\gamma, t_{\text{dif}}) = 2\sqrt{D(\gamma)t_{\text{dif}}[1 - (1 - \gamma/\gamma_{\text{max,halo}})/(1 - \delta)]}$. According to Atoyan et al. (1995), $\gamma_{\text{max,halo}} = 1/(p_2 t)$, and $\gamma_t = \gamma/(1 - p_2 t \gamma)$ represents the initial energy of electrons that have cooled to γ after time t , with p_2 being a coefficient for the synchrotron and IC loss rate influenced by the strength of the magnetic field B_{halo} (see Eq.(15) therein). For $\gamma < 0.5\gamma_{\text{max}}$, $r_{\text{dif}} \approx 2\sqrt{D(\gamma)t_{\text{dif}}}$.

The column density of electrons with energy γ at projection radius ρ is

$$N_{\text{LoS}}(\gamma, \rho, t_{\text{dif}}) = \int_{-\infty}^{\infty} f(\gamma, r, t_{\text{dif}}) dl = \int_{-\infty}^{\infty} \frac{\gamma_t^2 q_{\text{inj}}(\gamma_t, t_{\text{dif}})}{\gamma^2 \pi^{3/2} r_{\text{dif}}^3} \exp\left(-\frac{l^2 + \rho^2}{r_{\text{dif}}^2}\right) dl = \frac{\gamma_t^2 q_{\text{inj}}(\gamma_t, t_{\text{dif}})}{\gamma^2 \pi r_{\text{dif}}^2} \exp\left(-\frac{\rho^2}{r_{\text{dif}}^2}\right), \quad (4)$$

where $l = \sqrt{r^2 - \rho^2}$. For presenting γ -ray flux F_{halo} from the region within the projection radial size R_{halo} , we integrate F_{LoS} over the region after the injection time to get all of the historical contribution:

$$N_{\text{halo}} \propto \int_{t_{\text{disr}}}^{T_{\text{age}}} \int_0^{R_{\text{halo}}} N_{\text{LoS}} 2\pi \rho d\rho dt_{\text{dif}} = \frac{\gamma_t^2 q_{\text{A}} (\gamma_t/10^7)^{-\alpha_{\text{A}}}}{\gamma^2} \left[1 - \exp\left(-\frac{D^2}{r_{\text{dif}}^2(\gamma, T_{\text{age}} - t_{\text{cr}})}\right) \right]. \quad (5)$$

We calculate the diffusion of the very high-energy electrons that escaped ‘‘impulsively’’ when the reverse-shocked PWN was disrupted and their γ -ray SED. With the parameter values of D_0 , α_{A} , t_{disr} and q_{A} (as listed in Table 1), we calculate the distribution function of the electrons, $f(\gamma, r, t_{\text{dif}})$. Then we calculate the γ -ray SED of the injected high-energy electrons with parameter values of B_{halo} , R_{halo} , T_{age} , energy densities of intervening FIR, NIR and CMB photons (also see Table 1). As shown in Figure 2a, the model calculation can explain the γ -ray fluxes of HESS J1809–193 between 0.3 TeV to 30 TeV. The normalized diffusion coefficient $D_0 = 1.1 \times 10^{28} \text{ cm}^2 \text{ s}^{-1}$ is adopted from H. E. S. S. Collaboration et al. (2023) and is consistent with the slow diffusion hypothesis in Abeysekara et al. (2017).

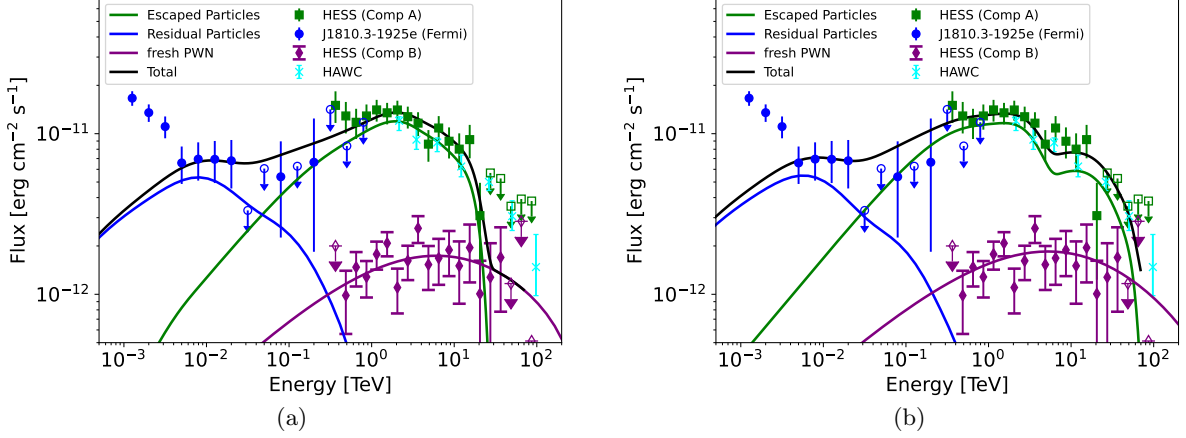


Figure 2. GeV-TeV γ -ray SED of HESS J1809–193. Contributions of three components of electrons are shown: (1) electrons escaped at disruption (for HESS component A, in green), remaining electrons after disruption (for Fermi-detected J1810.3–1925e arising from relic PWN, in blue), and electrons injected after disruption (for HESS component B, in purple), respectively (Araya 2018; H. E. S. S. Collaboration et al. 2023). The HAWC data points (shown for comparison only) are taken from Goodman (2022). (a) Used parameters are all given in Table 1. (b) Same as in (a), except $\alpha_{A1} = 1.75$ and $\alpha_{A2} = 1.88$ in the broken power law for injection rate (Eq. 15), as well as $B_{\text{Halo}} = 2.2 \mu\text{G}$.

Index $\alpha_A = 1.8$ is the best-fit value here for the TeV emission. We have also used broken power-law spectrum to fit the SED, but it resulted in little essential difference and improvement below 30 TeV.

Data at the highest energies reported by the HAWC collaboration (Albert et al. 2024) will be discussed below (see §3.2).

2.3. Remaining particles and the GeV gamma-rays

While the relic PWN was displaced from the pulsar by reverse shock, the remaining plasma experienced compression as aforementioned, and the high-energy electrons are postulated burnt off by a strong magnetic field enhanced by compression. Their energies are cut off at the Lorentz factor γ_{cut} due to significant synchrotron losses. The distribution function of the remaining electrons in the relic PWN, $G(\gamma, t)$, is derived by solving the electrons in number conservation equation

$$\frac{\partial G(\gamma, t)}{\partial t} = -\frac{\partial}{\partial \gamma} [\dot{\gamma}(\gamma, t)G(\gamma, t)] + Q_{\text{rem}}(\gamma, t), \quad (6)$$

and the injection rate (differential electron number per unit time) of the plasma that were emanated from the pulsar prior to disruption and remained later in the relic PWN is assumed as

$$Q_{\text{rem}}(\gamma, t) = \begin{cases} Q_{\text{pairs}}(\gamma, t)(\gamma/\gamma_{\text{break}})^{-\alpha_1}, & \gamma < \gamma_{\text{break}} \\ Q_{\text{pairs}}(\gamma, t)(\gamma/\gamma_{\text{break}})^{-\alpha_2}, & \gamma > \gamma_{\text{break}} \end{cases}, \quad (7)$$

where Q_{pairs} is a normalization constant and α_1 and α_2 are the spectral indices of the injected electrons. The rate of total electron energy injection into the PWN prior to disruption is expressed as

$$(1 - \eta)L(t) = \frac{(1 - \eta)L_0}{(1 + \frac{t}{\tau_0})^{(n+1)/(n-1)}} = \int_1^{\gamma_{\text{max, relic}}} Q_{\text{rem}}(\gamma, t)\gamma m_e c^2 d\gamma, \quad t \leq t_{\text{disr}}, \quad (8)$$

where L_0 is the initial spin-down luminosity, η the fraction of the spin-down energy deposited into magnetic field, n is the braking index, $\tau_0 = 2\tau_c/(n-1) - T_{\text{age}}$ is the initial spin down age of the pulsar. The electron's energy loss rate $\dot{\gamma}$ in Equation 6 is determined by synchrotron radiation, IC scattering (with CMB, FIR, and NIR photons), bremsstrahlung, and adiabatic losses. Integration limit $\gamma_{\text{max, relic}}$ in Equation 8 is treated similarly to $\gamma_{\text{max, halo}}$.

The magnetic field strength in the relic PWN is governed by the magnetic energy injected and its expansion (Tanaka & Takahara 2010):

$$\frac{dW_B(t)}{dt} = \eta L(t) - \frac{W_B(t)}{R_{\text{relic}}(t)} \frac{dR_{\text{relic}}(t)}{dt}, \quad t \leq t_{\text{disr}}, \quad (9)$$

Table 1. Model parameters

Par.	Description	Value
d (kpc)	distance to the pulsar	3.3 ^a
L (erg s ⁻¹)	pulsar spin-down power	1.8×10^{36a}
τ_c (kyr)	pulsar characteristic age	51.4 ^a
P (ms)	pulsar period	82.76 ^a
\dot{P} (s s ⁻¹)	pulsar period derivative	2.55×10^{-14a}
n	pulsar braking index	3 ^b
M_{ej} (M_{\odot})	ejecta mass	5 ^b
E_{SN} (erg)	supernova explosion energy	10^{51b}
δ	energy dependence of the diffusion index	0.58 ^c
D_0 (cm ² s ⁻¹)	diffusion coefficient normalized	1.1×10^{28c}
T_{NIR} (K)	NIR temperature	500 ^d
u_{NIR} (erg cm ⁻³)	NIR energy density	4×10^{-13d}
T_{FIR} (K)	FIR temperature	31.67 ^d
u_{FIR} (erg cm ⁻³)	FIR energy density	2.05×10^{-12d}
T_{CMB} (K)	CMB temperature	2.72 ^d
u_{CMB} (erg cm ⁻³)	CMB energy density	4.2×10^{-13d}
B_{halo} (μG)	field strength in the TeV halo	3.5 ^e
R_{halo} (pc)	radius of the TeV halo	23 ^c
q_{A} (cm ⁻³ s ⁻¹)	constant of injection into the halo	1.7×10^{37e}
η	magnetic fraction factor before disruption	0.07 ^e
γ_{break}	break energy of electrons in relic	9×10^{5e}
α_{A}	power-law index for injection into the halo	1.8 ^e
α_1	index in the broken power law	1.65 ^e
α_2	index in the broken power law	2.9 ^e
α_{B}	power-law index for injection after disruption	2.0 ^e
T_{age} (kyr)	age of the pulsar	40 ^e
n_{ISM} (cm ⁻³)	ISM number density	0.04 ^e
η_{post}	magnetic fraction factor after disruption	0.5 ^e
t_{disr} (kyr)	time when the PWN was disrupted	12 ^f

^a Adopted from Manchester et al. (2005)

^b Assumed value

^c Adopted from H. E. S. S. Collaboration et al. (2023)

^d Calculated from Popescu et al. (2017)

^e Fitted value

^f Calculated value

where $W_B(t)$ is the magnetic energy within the relic PWN, and $R_{\text{relic}}(t)$ is its radius (which is now 8 pc, see §2.1).

We first calculate the electrons injection rate Q_{rem} from Equation 8. Combining the radius evolution of the relic PWN that is obtained above (see §2.1 and Figure 1), we get the magnetic field evolution from Equation 9, which is used in calculating the energy loss rate $\dot{\gamma}$. Then we calculate the distribution function $G(\gamma, t)$ of the remaining particles from Equation 6. Finally we obtain the γ -ray SED of the remaining particles from $G(\gamma, t)$, incorporating energy densities of intervening FIR, NIR and CMB photons (also see Table 1). These calculations have used parameters L , τ_c , T_{age} , P , \dot{P} , n , η , α_1 , α_2 , along with energy densities of intervening FIR, NIR and CMB photons (as also listed in Table 1). As seen in Figure 2, the γ -ray emission arising from the remaining particles in the relic PWN is peaked at around 10 GeV. Combination of contributions from the relic PWN and the TeV halo can well explain the saddle-like SED of HESS J1809–193 from 5 GeV to 30 TeV, as well as the spectral hardening around 100 GeV. We note that, the index $\alpha_1 = 1.65$ below the break energy is similar to the index ($\alpha_{\text{A}} = 1.8$) of the electrons that were escaped into the halo.

In Equation 8, the high-energy particles that escaped have been ignored. Actually, the total energy of those particles, takes up only $\sim 6\%$ of the total energy of the particles injected prior to the disruption in this model calculation.

Regarding the emission below 5 GeV, in our model, the electron energy required to reproduce the observed flux through the IC process would exceed the pulsar’s injection energy, which is evidently unphysical. Several authors have proposed that it could originate from non-thermal bremsstrahlung interactions (Boxi & Gupta 2024; Albert et al. 2024), which agrees with our findings.

2.4. Post-disruption injection and HESS “component B”

After the PWN was disrupted by the reverse shock, the pulsar continues to inject high energy electrons, which then flow to the relic PWN through the newly formed cocoon. Hereby, we show that the γ -ray emission from the post-disruption electrons can be responsible for the compact TeV emission “component B”. We assume that the injection rate of the relativistic particles after disruption, $Q_{\text{post}}(\gamma, t)$, obeys a single power law:

$$Q_{\text{post}}(\gamma, t) = Q_{\text{B}}(t)\gamma^{-\alpha_{\text{B}}} \quad (\gamma < \gamma_{\text{post,max}}, t_{\text{disr}} < t \leq T_{\text{age}}), \quad (10)$$

where Q_{B} is the normalization coefficient. The upper cutoff $\gamma_{\text{post,max}}$ is obtained so as to confine the accelerated electrons within the PWN (Venter & de Jager 2007):

$$\gamma_{\text{post,max}} \approx \frac{e}{2m_e c^2} \sqrt{\frac{\sigma L(t)}{(1 + \sigma)c}}, \quad (11)$$

where the magnetization parameter σ is the ratio of the electromagnetic energy flux to the lepton energy flux and will be approximated here as $\eta_{\text{post}}/(1 - \eta_{\text{post}})$, with η_{post} the fraction of the spin-down energy deposited into magnetic field after disruption. The injection rate can be related to the spin-down power $L(t)$ at given time t by $(1 - \eta_{\text{post}})L(t) = \int Q_{\text{post}}(\gamma, t)\gamma m_e c^2 d\gamma$. Thus the normalization parameter $Q_{\text{B}}(t)$ can be derived as (Tanaka & Takahara 2010)

$$Q_{\text{B}}(t) = \frac{(1 - \eta_{\text{post}})L_0}{m_e c^2} \left(1 + \frac{t}{\tau_c}\right)^{-2} \left(\frac{\gamma_{\text{max}}^{2-\alpha_{\text{B}}} - 1}{2 - \alpha_{\text{B}}}\right)^{-1}. \quad (12)$$

On the assumption of magnetic field energy conservation, the time-varying field strength of the nebula is given by (see Tanaka & Takahara 2010)

$$B(t) = \sqrt{\frac{6\eta_{\text{post}}L_0 t_0}{R_{\text{PWN}}^3(t + t_0)}}, \quad (13)$$

where $R_{\text{PWN}}(t)$ is the mean radius of the PWN. The volume-integrated particle number $N(\gamma, t)$ as a function of energy and time is described by the continuity equation in the energy space:

$$\frac{\partial N(\gamma, t)}{\partial t} = -\frac{\partial}{\partial \gamma} [\dot{\gamma}(\gamma, t)N(\gamma, t)] + Q_{\text{post}}(\gamma, t). \quad (14)$$

In the above equation, particle escape in this stage is ignored because of longer escape time scale than that of this pulsar system.

With a similar algorithm to that used by Li et al. (2010), we have numerically calculated the SED of post-disruption PWN. Combining equations 10–12 and parameters of the PWN, we calculate the injection rate $Q_{\text{rem}}(\gamma, t)$. In the calculation, we approximate $R_{\text{PWN}}(t)$ as the radius of the re-expanding relic PWN $R_{\text{relic}}(t)$ (see Figure 1). Next, we calculate the magnetic field $B(t)$ via Equation 13. Then, combined with the parameters of PWN, such as L , τ_c , α_{B} , η_{post} , and energy densities (also see Table 1), we numerically solved for $N(\gamma, t)$ and calculate the SED of PWN. As shown in Figure 2a, the SED of HESS component B can be well fitted. The injection index $\alpha_{\text{B}} = 2$ is slightly larger than $\alpha_{\text{A}} = 1.8$.

On the other hand, hydrodynamic simulations of interaction between reverse shocks and PWNs show that the particles injected from pulsar into the relic PWN (via cocoon) after reverse-shock disruption will form a small central region of relatively high density, close to the injection site. This may imply that the emission of the electrons from the post-disruption injection will actually be brightened towards the central region of the relic PWN, appearing as a compact source, as described for HESS component B.

3. DISCUSSION

3.1. Radio traces of the parent SNR and the relic PWN?

Since PWN J1809–193 extends significantly beyond the two known nearby SNRs (G011.0–00.0 and G011.0+00.1), and no SNR spatially coincident with HESS J1809–193 has been observed yet, we need to check whether the discussed parent SNR of the PWN is elusive from radio detection due to its expansion in a low-density (of order $\sim 10^{-2} \text{ cm}^{-3}$) region. With the Sedov evolutionary law (Sedov 1958), we obtain the radius of the SNR at T_{age} (40 kyr) as $R_{\text{SNR}} = (2.026E_{\text{SN}}/1.4n_{\text{ISM}}m_{\text{H}})^{1/5}T_{\text{age}}^{2/5} \sim 40 \text{ pc}$ ($\sim 0^\circ.7$ in angular size), along with the expansion velocity $0.4R_{\text{SNR}}/T_{\text{age}} \sim 390 \text{ km s}^{-1}$.

We approximate the density distribution with radius for the gas inside the parent SNR as a power law with index 9. With the synchrotron emission coefficient given in Blumenthal & Gould (1970), we calculate the radio surface brightness distribution Σ at 1 GHz with the projection radius as plotted in Figure 3, wherein a total electron energy 10^{48} erg , distance $d \sim 3.3 \text{ kpc}$, and a magnetic field strength $10 \mu\text{G}$ are adopted. The brightness is within a range of $\sim 1 - 3 \times 10^4 \text{ Jy sr}^{-1}$. We alternatively use the NAIMA package (Zabalza 2015) to estimate the average radio surface brightness of the SNR at 1 GHz, which is $\sim 2 \times 10^4 \text{ Jy sr}^{-1}$.

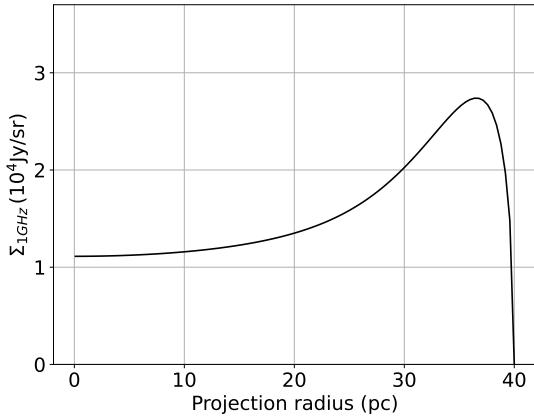


Figure 3. Model-predicted radio surface brightness of the parent SNR

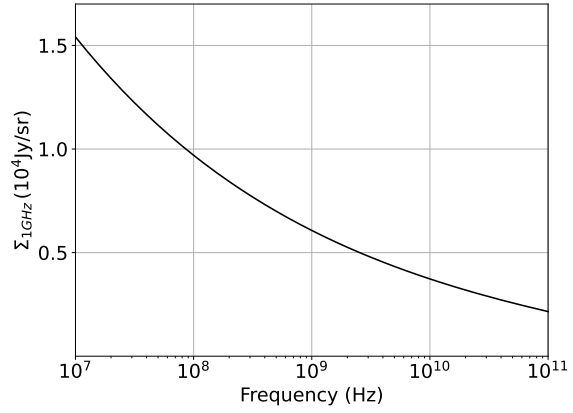


Figure 4. Model-predicted radio surface brightness of the relic PWN

With the scenario of reverse-shocked PWN to account for the γ -ray emission of HESS J1809–193, we also need to check whether there may be any visible trace of the relic PWN in radio observation. Based on the above results regarding the calculation of the electron energy distribution (including the remaining electrons and the post disruption injection) and the relic PWN radius (see §2.1 and §2.3), we can calculate its mean radio surface brightness profile, which is shown in Figure 4 to be of order 10^4 Jy sr^{-1} .

We have estimated the level of radio continuum emission in the background around HESS J1809–193, based on the 170 to 231 MHz radio-continuum emission data from the Galactic and Extragalactic All-sky Murchison Widefield Array survey. Four circular regions with faint emission, containing as little enhancement as possible, are selected to estimate the bottom level of background radio continuum emission. The total area of the background regions is comparable to that of the putative SNR. The background regions are close to, but outside of, the putative SNR, of which the central Galactic coordinates (l and b) and angular radius are $(10^\circ.66, 0^\circ.97, 0^\circ.34)$, $(10^\circ.85, -1^\circ.48, 0^\circ.34)$; $(11^\circ.49, 1^\circ.00, 0^\circ.34)$, and $(12^\circ.08, -0^\circ.96, 0^\circ.34)$, respectively. The surface brightness of the background is estimated as $\sim 5.0 \times 10^5 \text{ Jy sr}^{-1}$. The corresponding extrapolated 1 GHz surface brightness is estimated as $\sim 2.2 \times 10^5 \text{ Jy sr}^{-1}$, using a spectral index of -0.5 . The radio surface brightness of both of the parent SNR and the relic PWN are lower than the radio background brightness (see Figures 3 and 4). The variation of the background radio continuum emission is estimated as $\sim 2.7 \times 10^5 \text{ Jy sr}^{-1}$, and the extrapolated variation at 1 GHz becomes $\sim 1.2 \times 10^5 \text{ Jy sr}^{-1}$. By comparison, the radio continuum emissions from both the parent SNR and the relic PWN are actually submerged in the background.

3.2. HAWC detection above 100 TeV

Recently, HAWC reported detection of γ -ray flux above 100 TeV with no clear cutoff in the HESS J1809–193 region (Albert et al. 2024). Such a flux is not explained in the above modeling. In the framework of the modeling, this may indicate that there is also very high-energy particle injection in other ways. For example, X-ray filaments are observed extending from compact parts of PWNe, such as Guitar Nebula (e.g. de Vries et al. 2022), Lighthouse PWN (e.g. Klingler et al. 2023), etc. They are interpreted as beams of charge-separated very high-energy electrons or positrons (Olmi et al. 2024). In this scenario, non-resonant instability allows high-energy particles to propagate far from the pulsar along narrow channels in the ISM, forming elongated X-ray filaments and producing TeV halos that could reach up to 100 TeV or even higher (MAGIC Collaboration et al. 2023). In PWN J1809–193 (Klingler et al. 2020), a misaligned outflow structure of $\sim 7'$ in length was observed extending roughly perpendicular to the PWN’s central axis outside the compact nebula. It appears similar to the X-ray filaments observed in Guitar Nebula and Lighthouse PWN. Hence, this outflow structure could provide a potentially feasible explanation for additional high-energy electrons or positrons’ escape and generating a γ -ray flux exceeding 100 TeV.

However, the trend seen in HAWC data are similar to the flux level and slope of the TeV emission from component A. Therefore, it is also possible that the emission fluxes below and above 100 TeV have a common origin. In this case, we find that injection rate with a broken power law (instead of a single power law like Eq.1) could be capable of fitting the fluxes. Using injection rate given by

$$q_{\text{inj}}(\gamma) = \begin{cases} q_A \delta(t_{\text{dif}}) \left(\frac{\gamma}{10^7}\right)^{-\alpha_{A1}}, & \gamma < \gamma_{\text{break,Halo}} \\ q_A \delta(t_{\text{dif}}) \left(\frac{\gamma}{10^7}\right)^{-\alpha_{A2}}, & \gamma > \gamma_{\text{break,Halo}} \end{cases}, \quad (15)$$

the SED from GeV to above 100 TeV is fitted with parameters $\alpha_{A1} = 1.75$, $\alpha_{A2} = 1.88$ and $\gamma_{\text{break,Halo}} = 1.9 \times 10^7$, as well as magnetic field strength $2.2 \mu\text{G}$ (see Figure 2b). Though, this leads to a deviation of the flux in the energy interval 30–200 GeV. Also, the fitted field strength is even somewhat weaker than the interstellar average ($3 \mu\text{G}$), and the break energy $\gamma_{\text{break,Halo}}$ is an order of magnitude larger than that typically seen in PWNe ($\sim 10^6$ (Bucciantini et al. 2010)).

3.3. Comparison with previous explanations

While pointing out the difficulties with hadronic and lepto-hadronic hybrid models (also see mentioning in §1), H. E. S. S. Collaboration et al. (2023) propose a purely leptonic model to explain the emissions of HESS J1809–193. In the model, HESS component A is ascribed to the electrons injected over the lifetime of the system, and component B to ‘medium-age’ electrons that have been injected within the last ~ 5 kyr (without explaining physical origin). The model requires an additional IC component, emitted by electrons even older than the lifetime to account for the observed ~ 10 GeV γ -ray flux from J1810.3–1925e. In our model with the scenario of reverse-shocked PWN, these three γ -ray components can be explained with the leptonic emissions of three populations of electrons (§2.2, §2.3, and §2.4) related to the PWN evolution. We note that, with different origin mechanism, our calculation of post-disruption electron population described in §2.4 is somewhat similar to the calculation for component B (including power-law index and magnetic energy fraction) in H. E. S. S. Collaboration et al. (2023).

The lepto-hadronic hybrid explanation proposed by Boxi & Gupta (2024) and Albert et al. (2024) ascribe the TeV halo (HESS component A) to hadronic interaction of SNRs G11.0–0.0 and G11.0+0.1 with molecular clouds, and HESS component B to IC scattering of the CMB photons by the PWN electrons. This model can explain the measured HAWC flux points up to 200 TeV, but seriously overestimates the flux between 5 – 200 GeV, of Fermi-LAT detected J1810.3–1925e (H. E. S. S. Collaboration et al. 2023). Martin et al. (2024) suggest that component A can be attributed to escape of particles out of the nebula into the parent remnant and subsequently to the surrounding ISM, and component B can be associated with PWN or hadronic cosmic rays interacting with nearby molecular clouds, however their model needs another component to explain the emission below 10 GeV. By comparison to these explanations, our model explanation does not invoke hadronic interaction but only considers the effects of the PWN evolution in the parent SNR. We do not model the flux beyond 100 TeV but imply that it is caused by additional injection from the PWN, which should be tested with further observations.

4. CONCLUSION

For GeV-TeV source HESS J1809–193 together with J1810.3–1925e, we suggest that it is very likely to be PWN J1809–1917 observed in γ -ray emission. Based on evolutionary theory of PWNe, we consider that the PWN was

collided by the reverse shock moving inwards from the side with relatively dense ambient medium, roughly along the line of sight. Some very high-energy electrons escaped impulsively when the SNR was disrupted, and the other electrons remained in the relic PWN that was driven to the other side. The very high-energy part of the remaining electrons were burnt off by the strong magnetic field that was caused by the reverse shock compression in the reverberation stage, leaving the other part of them generating GeV emission. The particles injected from the pulsar after the disruption enter the relic PWN through the newly formed tunnel (called the cocoon). The γ -ray emission arising from the escaped part of electrons can account for the TeV SED of the HESS component A (namely, the TeV halo), and the electrons remaining after disruption account for the GeV SED emission of J1810.3–1925e. Summation of contributions from these two populations of electrons reproduces the saddle-like SED of HESS J1809–193 from 5 GeV to 30 TeV, as well as the spectral hardening around 100 GeV. The post-disruption injection of electrons is shown to be responsible for the relatively faint γ -ray emission of HESS component B. We also show that the radio emission from the PWN’s parent SNR, which is assumed to expand in a low-density ISM, and that from the relic PWN are both submerged in the radio background and are thus undetectable.

The emission flux above 100 TeV newly detected by HAWC from component A could be explained if either a very low field strength (smaller than the interstellar average) and an extraordinarily high break energy of the escaped electrons are invoked, or additional very-high energy injection is present, such as beam-like electrons injected from the compact nebula due to electron NRI along magnetic field lines.

5. ACKNOWLEDGMENTS

The authors thank Keping Qiu, Zhi-Yu Zhang, and Ruo-Yu Liu for helpful advice. Y.C. acknowledges the support from NSFC under grants 12173018, 12121003, and 12393852.

REFERENCES

- Abeyssekara, A. U., Albert, A., Alfaro, R., et al. 2017, *Science*, 358, 911, doi: [10.1126/science.aan4880](https://doi.org/10.1126/science.aan4880)
- . 2020a, *PhRvL*, 124, 021102, doi: [10.1103/PhysRevLett.124.021102](https://doi.org/10.1103/PhysRevLett.124.021102)
- . 2020b, *PhRvL*, 124, 021102, doi: [10.1103/PhysRevLett.124.021102](https://doi.org/10.1103/PhysRevLett.124.021102)
- Aharonian, F., Akhperjanian, A. G., Bazer-Bachi, A. R., et al. 2007, *A&A*, 472, 489, doi: [10.1051/0004-6361:20077280](https://doi.org/10.1051/0004-6361:20077280)
- Albert, A., Alfaro, R., Alvarez, C., et al. 2024, *ApJ*, 972, 21, doi: [10.3847/1538-4357/ad59a6](https://doi.org/10.3847/1538-4357/ad59a6)
- Alford, J. A., & Halpern, J. P. 2016, *The Astrophysical Journal*, 818, 122
- Anada, T., Bamba, A., Ebisawa, K., & Dotani, T. 2010, *PASJ*, 62, 179, doi: [10.1093/pasj/62.1.179](https://doi.org/10.1093/pasj/62.1.179)
- Araya, M. 2018, *ApJ*, 859, 69, doi: [10.3847/1538-4357/aabd7e](https://doi.org/10.3847/1538-4357/aabd7e)
- Atoyan, A. M., Aharonian, F. A., & Völk, H. J. 1995, *PhRvD*, 52, 3265, doi: [10.1103/PhysRevD.52.3265](https://doi.org/10.1103/PhysRevD.52.3265)
- Bandiera, R., Bucciantini, N., Martín, J., Olmi, B., & Torres, D. F. 2020, *MNRAS*, 499, 2051, doi: [10.1093/mnras/staa2956](https://doi.org/10.1093/mnras/staa2956)
- . 2023, *MNRAS*, 520, 2451, doi: [10.1093/mnras/stad134](https://doi.org/10.1093/mnras/stad134)
- Bao, Y., & Chen, Y. 2019, *ApJ*, 881, 148, doi: [10.3847/1538-4357/ab2ed8](https://doi.org/10.3847/1538-4357/ab2ed8)
- Bao, Y., Liu, S., & Chen, Y. 2019, *ApJ*, 877, 54, doi: [10.3847/1538-4357/ab1908](https://doi.org/10.3847/1538-4357/ab1908)
- Blumenthal, G. R., & Gould, R. J. 1970, *Reviews of Modern Physics*, 42, 237, doi: [10.1103/RevModPhys.42.237](https://doi.org/10.1103/RevModPhys.42.237)
- Boxi, S., & Gupta, N. 2024, *ApJ*, 961, 61, doi: [10.3847/1538-4357/ad0da9](https://doi.org/10.3847/1538-4357/ad0da9)
- Brogan, C. L., Gelfand, J., Gaensler, B. M., Kassim, N. E., & Lazio, T. J. 2006, *National Radio Astronomy Observatory Newsletter*, 108, 4
- Bucciantini, N., Arons, J., & Amato, E. 2010, *Monthly Notices of the Royal Astronomical Society*, 410, 381, doi: [10.1111/j.1365-2966.2010.17449.x](https://doi.org/10.1111/j.1365-2966.2010.17449.x)
- Castelletti, G., Giacani, E., & Petriella, A. 2016, *A&A*, 587, A71, doi: [10.1051/0004-6361/201527578](https://doi.org/10.1051/0004-6361/201527578)
- de Vries, M., Romani, R. W., Kargaltsev, O., et al. 2022, *ApJ*, 939, 70, doi: [10.3847/1538-4357/ac9794](https://doi.org/10.3847/1538-4357/ac9794)
- Gaensler, B. M., & Slane, P. O. 2006, *Annual Review of Astronomy and Astrophysics*, 44, 17–47, doi: [10.1146/annurev.astro.44.051905.092528](https://doi.org/10.1146/annurev.astro.44.051905.092528)
- Goodman, J. 2022, Presentation at Gamma 2022 Conference, <https://indico.icc.ub.edu/event/46/contributions/1375/attachments/428/802/Goodman%20Barcelona%202022.pdf>
- Green, D. A. 2004, *Bulletin of the Astronomical Society of India*, 32, 335, doi: [10.48550/arXiv.astro-ph/0411083](https://doi.org/10.48550/arXiv.astro-ph/0411083)

- H. E. S. S. Collaboration, Aharonian, F., Ait Benkhali, F., et al. 2023, *A&A*, 672, A103, doi: [10.1051/0004-6361/202245459](https://doi.org/10.1051/0004-6361/202245459)
- Hinton, J. A., Funk, S., Parsons, R. D., & Ohm, S. 2011, *ApJL*, 743, L7, doi: [10.1088/2041-8205/743/1/L7](https://doi.org/10.1088/2041-8205/743/1/L7)
- Kargaltsev, O., & Pavlov, G. G. 2007, *ApJ*, 670, 655, doi: [10.1086/521814](https://doi.org/10.1086/521814)
- Klingler, N., Hare, J., Kargaltsev, O., Pavlov, G. G., & Tomsick, J. 2023, *The Astrophysical Journal*, 950, 177, doi: [10.3847/1538-4357/accd60](https://doi.org/10.3847/1538-4357/accd60)
- Klingler, N., Kargaltsev, O., Pavlov, G. G., & Posselt, B. 2018, *ApJ*, 868, 119, doi: [10.3847/1538-4357/aae0f1](https://doi.org/10.3847/1538-4357/aae0f1)
- Klingler, N., Yang, H., Hare, J., et al. 2020, *ApJ*, 901, 157, doi: [10.3847/1538-4357/abaf4b](https://doi.org/10.3847/1538-4357/abaf4b)
- Klingler, N., Yang, H., Hare, J., et al. 2020, *The Astrophysical Journal*, 901, 157, doi: [10.3847/1538-4357/abaf4b](https://doi.org/10.3847/1538-4357/abaf4b)
- Komin, N., Carrigan, S., Djannati-Ataï, A., et al. 2008, in *International Cosmic Ray Conference*, Vol. 2, International Cosmic Ray Conference, 815–818, doi: [10.48550/arXiv.0709.2432](https://doi.org/10.48550/arXiv.0709.2432)
- Li, C.-M., Ge, C., & Liu, R.-Y. 2023, *ApJ*, 949, 90, doi: [10.3847/1538-4357/acc7a0](https://doi.org/10.3847/1538-4357/acc7a0)
- Li, H., Chen, Y., & Zhang, L. 2010, *MNRAS*, 408, L80, doi: [10.1111/j.1745-3933.2010.00934.x](https://doi.org/10.1111/j.1745-3933.2010.00934.x)
- Maan, Y., Surnis, M. P., Chandra Joshi, B., & Bagchi, M. 2022, *ApJ*, 931, 67, doi: [10.3847/1538-4357/ac68f1](https://doi.org/10.3847/1538-4357/ac68f1)
- MAGIC Collaboration, Acciari, V. A., Ansoldi, S., et al. 2023, *A&A*, 670, A8, doi: [10.1051/0004-6361/202038748](https://doi.org/10.1051/0004-6361/202038748)
- Manchester, R. N., Hobbs, G. B., Teoh, A., & Hobbs, M. 2005, *AJ*, 129, 1993, doi: [10.1086/428488](https://doi.org/10.1086/428488)
- Martin, P., de Guillebon, L., Collard, E., et al. 2024, *A&A*, 690, A116, doi: [10.1051/0004-6361/202450254](https://doi.org/10.1051/0004-6361/202450254)
- Olmi, B., Amato, E., Bandiera, R., & Blasi, P. 2024, *A&A*, 684, L1, doi: [10.1051/0004-6361/202449382](https://doi.org/10.1051/0004-6361/202449382)
- Popescu, C. C., Yang, R., Tuffs, R. J., et al. 2017, *MNRAS*, 470, 2539, doi: [10.1093/mnras/stx1282](https://doi.org/10.1093/mnras/stx1282)
- Renaud, M., Hoppe, S., Komin, N., et al. 2008, in *American Institute of Physics Conference Series*, Vol. 1085, American Institute of Physics Conference Series, ed. F. A. Aharonian, W. Hofmann, & F. Rieger (AIP), 285–288, doi: [10.1063/1.3076661](https://doi.org/10.1063/1.3076661)
- Sedov, L. I. 1958, *Reviews of Modern Physics*, 30, 1077, doi: [10.1103/RevModPhys.30.1077](https://doi.org/10.1103/RevModPhys.30.1077)
- Slane, P., Lovchinsky, I., Kolb, C., et al. 2018, *ApJ*, 865, 86, doi: [10.3847/1538-4357/aada12](https://doi.org/10.3847/1538-4357/aada12)
- Tanaka, S. J., & Takahara, F. 2010, *ApJ*, 715, 1248, doi: [10.1088/0004-637X/715/2/1248](https://doi.org/10.1088/0004-637X/715/2/1248)
- Temim, T., Slane, P., Kolb, C., et al. 2015, *ApJ*, 808, 100, doi: [10.1088/0004-637X/808/1/100](https://doi.org/10.1088/0004-637X/808/1/100)
- Tibaldo, L., Zanin, R., Faggioli, G., et al. 2018, *A&A*, 617, A78, doi: [10.1051/0004-6361/201833356](https://doi.org/10.1051/0004-6361/201833356)
- Truelove, J. K., & McKee, C. F. 1999, *ApJS*, 120, 299, doi: [10.1086/313176](https://doi.org/10.1086/313176)
- Venter, C., & de Jager, O. C. 2007, in *WE-Heraeus Seminar on Neutron Stars and Pulsars 40 years after the Discovery*, ed. W. Becker & H. H. Huang, 40, doi: [10.48550/arXiv.astro-ph/0612652](https://doi.org/10.48550/arXiv.astro-ph/0612652)
- Voisin, F. J., Rowell, G. P., Burton, M. G., et al. 2019, *PASA*, 36, e014, doi: [10.1017/pasa.2019.7](https://doi.org/10.1017/pasa.2019.7)
- Zabalza, V. 2015, *Proc. of International Cosmic Ray Conference 2015*, 922